International Journal of Nanomedicine

Dovepress
open access to scientific and medical research

Open Access Full Text Article

ORIGINAL RESEARCH

Ultrasound Assisted a Peroxisome Proliferator-Activated Receptor (PPAR)γ Agonist-Loaded Nanoparticle-Microbubble Complex to Attenuate Renal Interstitial Fibrosis

This article was published in the following Dove Press journal:
International Journal of Nanomedicine

Shuping Wei[1]
Chaoli Xu[2]
Yidan Zhang[1]
Zhongqing Shi[3]
Min Wu[1]
Bin Yang[2]

[1]Department of Ultrasound, Nanjing Drum Tower Hospital, The Affiliated Hospital of Nanjing University Medical School, Nanjing, Jiangsu, People's Republic of China; [2]Department of Ultrasound, Jinling Hospital, Medical School of Nanjing University, Nanjing, Jiangsu, People's Republic of China; [3]Department of Cardiac Function, Nanjing Drum Tower Hospital, The Affiliated Hospital of Nanjing University Medical School, Nanjing, Jiangsu, People's Republic of China

Correspondence: Bin Yang
Department of Ultrasound, Jinling Hospital, Medical School of Nanjing University, 305 Zhongshan East Road, Nanjing, Jiangsu 210002, People's Republic of China
Tel +86-025-80861314
Email yangbin12yx@163.com

Min Wu
Department of Ultrasound, Nanjing Drum Tower Hospital, The Affiliated Hospital of Nanjing University Medical School, 321 Zhongshan Road, Nanjing, Jiangsu 210009, People's Republic of China
Tel +86-025-83304616
Email wuminguyi@163.com

Objective: To investigate the antifibrotic effect of the combination of a PPARγ agonist-loaded nanoparticle-microbubble complex with ultrasound (US) exposure on renal interstitial fibrosis (RIF).

Materials and Methods: Polylactide-co-glycolide (PLGA) nanoparticles were used to load PPARγ agonist (rosiglitazone, RSG) and prepare PLGA-RSG nanoparticles (PLNPs-RSG); then, a novel complex between PLNPs-RSG and SonoVue microbubbles (MBs) (PLNPs-RSG-MBs) was prepared. The size distribution, zeta potentials, RSG-loading capacity and entrapment efficiency were measured, and the release of RSG was assessed using a UV-vis spectrophotometer. The in vitro cytotoxicity and in vivo systemic toxicity assays were performed. The cellular uptake assessment was performed using a confocal laser scanning microscope (CLSM). The in vivo biodistribution assessment was performed using fluorescence imaging with a near-infrared (NIR) imaging system. Furthermore, this complex was administered to a unilateral ureteral obstruction (UUO) rat model with the assistance of US exposure to investigate the antifibrotic effect.

Results: This PLNPs-RSG-MBs complex had a size of 2199.5± 988.1 nm and a drug-loading efficiency of 28.5%. In vitro cytotoxicity and in vivo systemic toxicity assays indicated that the PLNPs-RSG-MBs complex displayed excellent biocompatibility. In addition, the complex showed high cellular uptake efficiency in vitro and kidney-targeting ability in vivo. In a UUO rat model, the combination of the PLNPs-RSG-MBs complex with US exposure significantly reduced collagen deposition and successfully attenuated renal fibrosis.

Conclusion: The combination of the PLNPs-RSG-MBs complex with US exposure may be a promising approach for the treatment of RIF.

Keywords: ultrasound, nanoparticles, microbubbles, peroxisome proliferator-activated receptor, renal interstitial fibrosis

Introduction

Chronic kidney disease (CKD) has become a serious health and socioeconomic problem in recent years. Renal interstitial fibrosis (RIF) is a common final pathway in the progression of almost all types of CKD to end-stage renal disease (ESRD). Thus, effective inhibition of renal fibrosis may be a pivotal strategy to prevent the progression of CKD.

submit your manuscript | www.dovepress.com
DovePress
http://doi.org/10.2147/IJN.S262052

RIF is characterized as the proliferation of renal interstitial fibroblasts and the accumulation of extracellular matrix (ECM), which is mainly mediated by transforming growth factor-β1 (TGF-β1) signaling pathways. PPARγ is a ligand-specific transcription factor that is selectively expressed in the medullary collecting duct, glomeruli, and proximal tubular cells in the kidney.[1] Activated PPARγ can significantly inhibit the secretion of inflammatory cytokines and prevent ECM synthesis by inhibiting the TGF-β1 signaling pathway, the anti-inflammatory and antifibrotic effects of which are manifested in various kidney diseases.[2,3] Thiazolidinediones (TZDs), such as rosiglitazone (RSG) and pioglitazone, are exogenous agonists of PPARγ, and many recent studies have shown that treatment with TZDs exerts a renoprotective effect and further delays the progression of CKD to RIF.[4,5] However, due to their poor water solubility and short circulating half-lives, the bioavailability of these drugs is low; moreover, these drugs have some potential side effects, such as hepatotoxicity, fluid retention, and increased risks of congestive heart failure, myocardial infarction and bladder cancer, which limit their clinical application.[6,7] Therefore, a novel targeted drug delivery strategy should be developed to improve the specific therapeutic effect and reduce the side effects of these drugs.

The use of ultrasound-targeted microbubble destruction (UTMD)-mediated drug-targeted delivery and gene transfection is a new approach that has been applied in many studies, including in the treatment of various kidney diseases.[8–10] Microbubbles (MBs) exposed to ultrasound (US) in a field mediates sonoporation, which temporarily increases the permeabilization of cellular membranes or the microvasculature only at the target site; thus, this technique effectively promotes the intracellular uptake of genes or drugs and reduces undesirable side effects.[11] In the kidney, UTMD increases the permeability of renal interstitial capillaries without inducing glomerular injury,-[12,13] indicating that this technology is feasible for application in the kidney. However, some limitations of using MBs as an efficient vehicle to carry drugs have been identified. Due to the thin shell and gaseous core of MBs, their drug-loading capacity is low; in addition, the difficulty in controlling drug release and the short circulation time of MBs in vivo would not result in an efficient therapy.[14] In contrast, nanoparticles have the advantages of an increased drug-loading capacity, prolonged action time and sustained drug release; moreover, they display good biocompatibility and biodegradation. Thus, as nanoparticles provide other functions than MBs, a promising approach is to develop MBs integrated with drug-loaded nanoparticles.[15] In recent years, the use of nanoparticles as coating materials for MBs has attracted increasing attention in many studies.[16–18] To the best of our knowledge, there is no study to date combining US exposure with MB-coupled drug-loaded nanoparticles for the treatment of renal diseases.

Polylactide-co-glycolide (PLGA) is a common biodegradable material that has been approved by the US Food and Drug Administration for widely used in clinical applications; PLGA nanoparticles (PLNPs) have been extensively studied as drug delivery vehicles and also been used to treat renal fibrosis.[19] However, the negative charge of unmodified PLNPs often limits their adjuvant activity.[20] As a widely used cationic polymer, polyethyleneimine (PEI) has been used to modify the surface charge of PLNPs.[21,22] Therefore, in this study, we used PLNPs to load the PPARγ agonist RSG and prepare PLGA-RSG nanoparticles (PLNPs-RSG). Furthermore, the PLNPs-RSG were modified by coupling with PEI to fabricate cationic PLNPs-RSG. In addition, freeze-dried commercial SonoVue powder coated with a thin lipid monolayer membrane shell and containing sulfur hexafluoride-filled MBs was used, as the surface charge of SonoVue MBs is negative,[23] the cationic PLNPs-RSG were conjugated with the MBs to synthesize a novel PLNPs-RSG-MBs complex via electrostatic interactions (Figure 1A) with a conjugation method similar to the protocol described in a previous study.[24] Furthermore, this complex was administered to a unilateral ureteral obstruction (UUO) rat model with the assistance of US exposure, and the purpose of this study was to investigate its antifibrotic effect on RIF (Figure 1B).

Materials and Methods

Materials

PLGA (50:50) was purchased from Jinan Daigang Biomaterial Co., Ltd. (China). RSG was purchased from Aladdin Industrial Corporation (Shanghai, China). Dichloromethane (DCM) was obtained from Nanjing Ningshi Chemical Reagent Co., Ltd. (China). PEI (branched, Mw: 25,000) was purchased from Sigma-Aldrich (St. Louis, MO, USA). Polyvinylpyrrolidone (PVP) and 3-(4,5-dimethylthiazol-2-yl)-2,5-diphenyltetrazolium bromide (MTT) were obtained from Sinopharm Chemical Reagent Co., Ltd. (Shanghai, China). Isopropyl

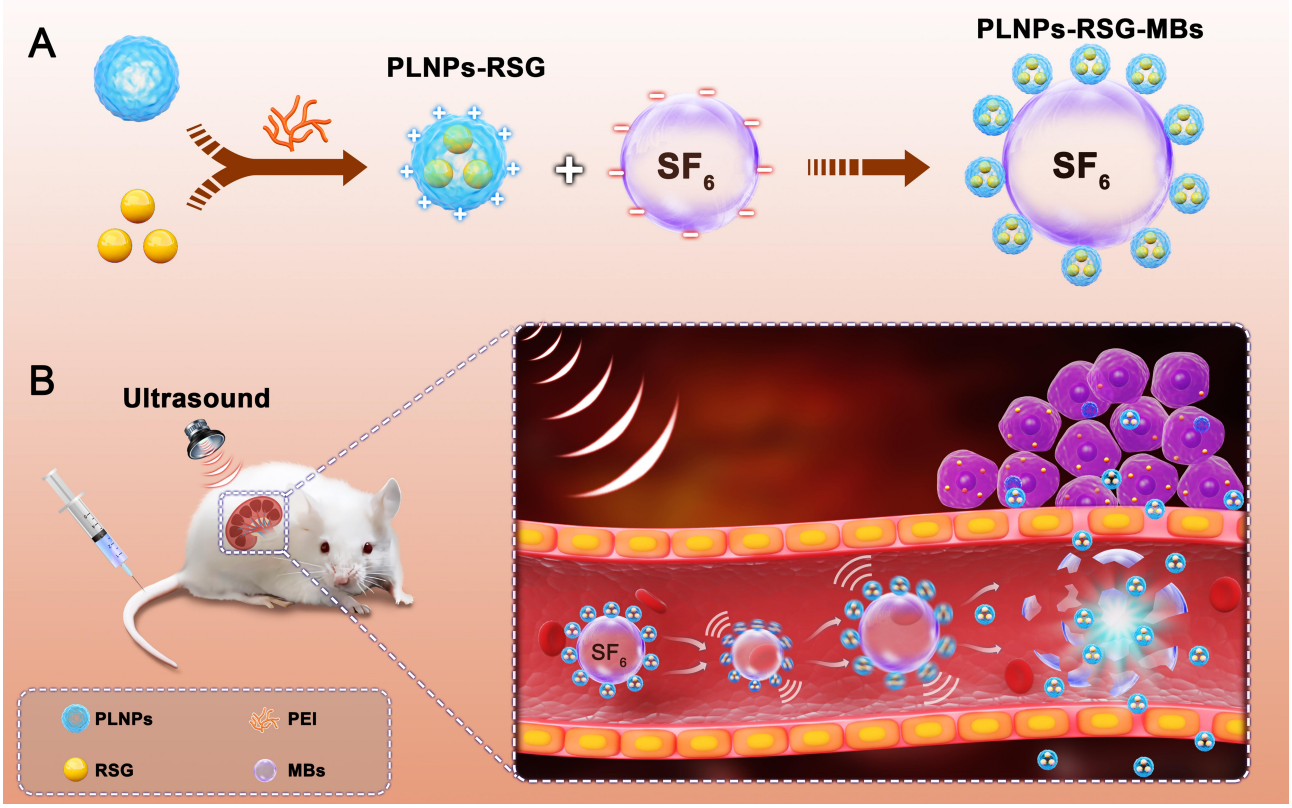

Figure 1 (**A**) Schematic illustration of PLNPs-RSG-MBs complex synthesis. (**B**) Schematic illustration of improved drug delivery to a UUO rat kidney due to the combination of the PLNPs-RSG-MBs complex with US exposure.

alcohol and N, N-dimethylformamide (DMF) were obtained from Nanjing Chemical Reagent Co., Ltd. (China). Cyanine 5.5 carboxylic acid (Cy5.5-COOH, Mw: 619.23) was purchased from J&K Scientific Inc. (Beijing, China). 4′-6-Diamidino-2-phenylindole (DAPI) and Dulbecco's Modified Eagle's Medium (DMEM) were obtained from Nanjing Keygen Biotech. Co., Ltd. (China). The contrast agent SonoVue was obtained from Bracco (Milan, Italy). Fetal bovine serum (FBS), trypsin, and dimethyl sulfoxide (DMSO) were obtained from Gibco/Life Technologies (Grand Island, New York, USA). SDS-PAGE gels and the primary antibodies used in this study were obtained from Servicebio Technology Co., Ltd. (Wuhan, China). Polyvinylidene fluoride (PVDF) membranes were obtained from Millipore (USA). A RevertAid First Strand cDNA Synthesis Kit was obtained from Thermo Scientific (USA). FastStart Universal SYBR Green Master (Rox) was obtained from Roche Co., Ltd. (Basel, Switzerland). Mouse mesangial cells (SV40-MES-13) were purchased from Shanghai Fuheng Biology Co., Ltd. (China).

Synthesis of PLNPs-RSG

The PLNPs were synthesized using methods described in a previous study with slight modifications.[25] In brief, 50 mg of PLGA was dissolved in 2 mL of DCM, and the mixture was emulsified by sonication for 3 min (on and off at 3-s intervals, 100 W) in an ice water bath to form a primary emulsion (W/O). Then, the solution was mixed with 6 mL of a 4% PVP solution and sonicated for 3 min (on and off at 3-s intervals, 100 W) to obtain the second emulsion (W/O/W). Next, the resultant emulsion was poured into an isopropyl alcohol solution (6 mL, 2%) and magnetically stirred for 4 h at the optimum temperature for the complete removal of dichloromethane. Finally, the PLNPs were purified by centrifugation (4000 rpm, 5 min) and dispersed in water. The RSG-loaded PLNPs (PLNPs-RSG) were obtained using the same method, except that 25 mg of RSG was added to the PLGA. Finally, the prepared nanoparticles were resuspended in deionized water, vacuum-dried for 24 h and stored at −20°C until further use.

Preparation of the PLNPs-RSG-MBs Complex

The PLNPs-RSG were modified by coupling with PEI onto the shell of the PLNPs-RSG to prepare the PLNPs-RSG-MBs complex. Briefly, 50 mg of the PLNPs-RSG suspension was added to a 5% PEI solution and incubated with gentle shaking for 4 h, washed 3 times and then resuspended in deionized water. The freeze-dried SonoVue powder was dissolved in 5 mL of normal saline according to the manufacturer's instructions. Afterwards, the PLNPs-RSG were dispersed in 1, 2.5, 5, and 10 mL of MBs (1 mg/mL) in phosphate-buffered saline (PBS) for 4 h and then washed once (1500 rpm, 5 min). The optimal conjugated PLNPs-RSG-MBs complex was chosen for further use.

Characterization of Different Preparations

The size distribution and zeta potentials of PLNPs-RSG, free MBs and the PLNPs-RSG-MBs complex were measured using a Zeta/PALS particle size and surface potential analyzer (Brookhaven Instruments). The morphologies of PLNPs-RSG, free MBs and the PLNPs-RSG-MBs complex were observed using an Olympus IX71 inverted microscope.

Drug Loading and Release

The RSG-loading capacity and entrapment efficiency were calculated by measuring free RSG concentrations in the supernatants using a UV-vis spectrophotometer (LAMBDA 35, Perkin-Elmer Instruments, USA). Through comparison with a standard curve generated from a series of RSG solutions at known concentrations, the following formulas were used to calculate the drug-loading capacity and entrapment efficiency: drug-loading capacity=(weight of RSG in preparations/weight of preparations) ×100% and entrapment efficiency=(weight of RSG in preparations/amount of RSG)×100%.

To analyze the release of RSG from the PLNPs-RSG-MBs complex, 1 mg of the PLNPs-RSG-MBs complex was incubated in PBS (1 mL, pH 7.4). The solution was exposed to the US at different powers (0, 1and 2 W/cm^2) and 1 MHz with a 50% duty cycle; the solution was sonicated for 10 s with a 10-s pause for a total of 5 min with a sonoporator (Sonitron 2000, Artison, OK, USA) for different time intervals. At the selected time points, 0.2 mL of the mixture was centrifuged to obtain the supernatant, which was analyzed at 350 nm using UV-vis spectroscopy.

Cell Culture

Mouse mesangial cells (SV40-MES-13) were incubated in DMEM supplemented with 10% FBS and 100 U/mL penicillin-streptomycin. All cells were cultured in a humidified environment containing 5% CO_2 at 37°C.

Cell Viability Assessment

SV40-MES-13 cells were seeded in 96-well plates at a density of 5×10^4 cells per well and incubated for 12 h. Afterwards, the cells were incubated with 100 μL of fresh medium containing various concentrations of the PLNPs, PLNPs-MBs, PLNPs-RSG or the PLNPs-RSG-MBs complex (0, 0.625, 1.25, 2.5, 5 or 10 μg/mL) for 24 h. Then, the cells were further incubated with fresh medium containing MTT (0.5 mg/mL) for 4 h. After removing the supernatant, 150 μL of DMSO was added to each well and then gently stirred for 10 min to solubilize the formazan crystals that formed in the well. The absorbance was measured at 570 nm with a microplate reader (Multiskan Ascent, Thermo Scientific), and cell viability was calculated as a percentage relative to the group grown in the culture medium.

Cellular Uptake Assessment

To prepare fluorescent PLNPs-RSG, 0.5 mg of Cy5.5 COOH was mixed with the initial PLNPs-RSG solution. The drug-loaded nanoparticles were synthesized as described above. SV40-MES-13 cells were plated in 6-well plates at a density of 1.5×10^6 cells per well, and the culture medium in each well was then replaced with 1 mL of fresh medium containing PLNPs-RSG-Cy5.5 or PLNPs-RSG-MBs-Cy5.5. US exposure was immediately added to the bottom of each well (1 MHz, 1.0 W/cm^2, 50% duty cycle, and sonication for 10 s with a 10-s pause for a total of 1 min), the groups that were not subjected to US exposure were used as controls. At 6 h after the incubation at 37°C, the treated cells were fixed with 4% paraformaldehyde for 20 min at 37°C and washed thrice with PBS. Then, DAPI was added to stain the cell nuclei, and the intracellular uptake of these materials was investigated with a Leica 21 TSC SP8 confocal laser scanning microscope (CLSM) (Germany). The average fluorescence intensity of nanoparticles in cells was calculated by measuring the integrated fluorescence density per area in three randomly selected fields (1024 × 1024 pixels) per slide (3

slides per experimental group), using Image-Pro Plus version 6.0 software (Media Cybernetics, Inc., Rockville, MD, USA).

In vivo Biocompatibility

Sprague-Dawley (SD) rats (male, 4–6 weeks old) weighing 180~200 g were used in the present study. The animals were housed in a temperature-controlled room, where they had free access to food and water. All procedures involving animals conformed to the institutional guidelines for the care and use of laboratory animals and were approved by the Laboratory Animal Ethics Committee of Jinling Hospital, Medical School of Nanjing University, where the study was performed.

After anesthetization with an intraperitoneal injection of 0.6 mL of 2% sodium pentobarbital, the SD rats were divided into two treatment groups and intravenously injected with PLNPs-RSG or the PLNPs-RSG-MBs complex (200 μL, 15 mg/mL). The body weights of all rats were measured over a 21-day period. Afterwards, the rats were sacrificed, and the major organs (the heart, liver, spleen, lung, and kidney) were stained with hematoxylin and eosin (H&E).

Renal Fibrosis Model of UUO

To induce a UUO rat model, the right ureter of each rat was ligated. The UUO model was generated as previously described.[26] The sham operation group was used as the control, in which the ureters of rats were exposed and operated on without ligation. The animals received treatment on the 3rd day after the UUO or sham operation.

In vivo Biodistribution

PLNPs-RSG-Cy5.5 or PLNPs-RSG-MBs-Cy5.5 were intravenously injected (200 μL, 15 mg/mL) into UUO rats. Local US exposure was applied to the right kidney using a Sonitron 2000 sonoporator (1 MHz, 1.5 W/cm^2, 50% duty cycle, and sonication for 10 s and with a 10-s pause for a total of 5 min), and animals without US exposure were used as the control cohorts (3 rats in each group). The rats were sacrificed at 24 h postinjection, and the major organs (the heart, liver, spleen, lung, and both kidneys) were harvested for fluorescence imaging using a near-infrared (NIR) imaging system (In Vivo Master, Wuhan Grand-imaging Technology Co. Ltd.) equipped with a thermoelectric cooled CCD camera. Excitation was provided by a 680-nm diode laser. The excitation intensity of the 680-nm laser was approximately 10 mW/cm^2. The emission light was filtered by a 730-nm bandpass filter. The mean fluorescence intensities of each kidney were calculated using ImageJ software (Rawak Software, Inc., Germany) to determine the relative ratio between the right and left kidneys.

Experimental Groups

The UUO rats were randomly divided into the following seven experimental groups (5 rats per group): group 1, the sham operation (sham group); group 2, the animals in which underwent UUO without any treatment (UUO group); group 3, the UUO model rats in which received PLNPs-RSG alone without US exposure (PLNPs-RSG group); group 4, the UUO model rats in which received PLNPs-RSG with US exposure (PLNPs-RSG+US group); group 5, the UUO model rats in which received the blank PLNPs-MBs complex without RSG followed by local US exposure (PLNPs-MBs+US group); group 6, the UUO model rats in which received the PLNPs-RSG-MBs complex without US exposure (PLNPs-RSG-MBs group); and group 7, the UUO model rats in which received the PLNPs-RSG-MBs complex followed by local US exposure (PLNPs-RSG-MBs+US group).

In vivo US Imaging and Drug Delivery

Each rat was anesthetized with an intraperitoneal injection of 0.6 mL of 2% sodium pentobarbital. The abdominal fur was removed using depilation. US imaging was performed using a Vinno 70 US scanner (Vinno Technology Co., Ltd., Suzhou, China) with an X4-12L linear transducer (10 MHz) to orient the kidney for subsequent US exposure. The transducer was coupled to the skin of the rats in the region of the right kidney via acoustic coupling gel. Firstly, conventional B-mode US scanning was performed to obtain the location, size and baseline echogenicity of the kidney. Then, contrast imaging mode was selected, and the gain settings were optimized to detect MBs without destruction. A mechanical index (MI) of 0.04 was used. Two hundred microliters of PLNPs-RSG, the PLNPs-MBs complex or the PLNPs-RSG-MBs complex (with an RSG concentration of 40 μg/mL and equivalent PLNPs-MBs complex concentrations of 20 μg/mL) were administered as a bolus via a tail vein injection daily for 7 days. Contrast-enhanced ultrasound (CEUS) imaging was performed both before and after US exposure to confirm the arrival and complete clearance of MBs in the kidney. US exposure was performed using a Sonitron 2000 sonoporator (1 MHz, 1.5 W/cm^2, 50% duty cycle, and sonication

for 10 s and with a 10-s pause for a total of 5 min). The sonoporation probe was located in the area of the right kidney, as confirmed by B-mode US imaging, and the arrival and clearance of MBs were observed using CEUS imaging.

All rats were euthanized and sacrificed at day 10 after the UUO operation, and their right kidneys were removed, fixed with 4% paraformaldehyde and embedded in paraffin for the histological examination or frozen in liquid nitrogen for fluorogenic quantitative RT-PCR and Western blotting.

Histology and Immunohistochemistry

H&E and Masson's trichrome staining were performed as described in a previous study.[27] The fibrotic area in three randomly selected fields (200×) of each kidney tissue section was quantified using Image-Pro Plus version 6.0 software to determine the amount of collagen deposition. In addition, paraffin-embedded tissue sections were subjected to immunohistochemical staining, and the sections were rehydrated and labeled with antibodies against TGF-β1, α-SMA, and Collagen I. The secondary antibody was biotinylated goat anti-rat IgG. The integrated optical density (IOD) in three randomly selected fields (200×) from each kidney tissue section was also quantitatively measured using Image-Pro Plus version 6.0 software.

Fluorogenic Quantitative RT-PCR

The fluorogenic quantitative RT-PCR analysis of PPARγ, TGF-β1, α-SMA, and Collagen I expression was performed as described previously.[27] Briefly, total RNA was extracted from the kidney tissues from the different groups using TRIzol reagent. Reverse transcription was conducted using a RevertAid First Strand cDNA Synthesis Kit. Quantitative RT-PCR was performed using FastStart Universal SYBR Green Master (Rox) according to the manufacturer's instructions. The mRNA levels of these genes were normalized to those of GAPDH and calculated using the standard ΔCt method. Sequences of the primers used in the experiments are shown in Table S1of the Supporting Information.

Western Blot Analysis

Total tissue proteins were extracted for Western blot analysis as described in a previous study.[27] Briefly, approximately 20 μg of protein from each sample was separated on 10% SDS-PAGE gels and then transferred to PVDF membranes. The membranes were incubated with primary antibodies against PPARγ, TGF-β1, α-SMA, Collagen I and β-actin overnight at 4°C. Afterwards, the membranes were incubated with a horseradish peroxidase-conjugated secondary antibody at room temperature for 1 h. The protein bands were analyzed with AlphaEaseFC (Alpha Innotech, San Leandro, CA, USA).

Statistical Analysis

Statistical calculations were performed using GraphPad Prism software (La Jolla, California, USA). Data are presented as the mean ± SD. Differences between the two groups were evaluated using the unpaired Student's *t*-test. A p value <0.05 indicated statistical significance.

Results and Discussion

Characterization of the Preparations

The inverted microscope images revealed a well-defined spherical shape of PLNPs-RSG, with a diameter of approximately 600 nm (Figure 2A). The PLNPs-RSG were then coated with a PEI layer to couple with MBs (which is shown in Figure 2B). The inverted microscope image of the PLNPs-RSG-MBs complex showed the PLNPs-RSG arranged around the MB in a ring (Figure 2C), suggesting the successful conjugation of PLNPs-RSG and MBs. The dynamic light scattering (DLS) analysis revealed that the hydrodynamic diameters of PLNPs-RSG, free MBs and the PLNPs-RSG-MBs complex were 632.8±38.6 nm, 1814.6±568.9 nm, and 2199.5±988.1 nm, respectively, suggesting a good uniformity and dispersity (Figure 2D). The hydrodynamic diameter of the PLNPs-RSG-MBs complex was larger than the free MBs, indicating the successful coupling of PLNPs-RSG to MBs. The zeta potentials of PLNPs-RSG, PLNPs-RSG-PEI, MBs, and PLNPs-RSG-MBs were −33.6 ± 4.6 mV, 40.5 ± 3.4 mV, −33.5 ± 2.8 mV, and-16.7 ± 2.6 mV, respectively (Figure 2E), indicating that the PEI-mediated cationic PLNPs-RSG were conjugated with the MBs via electrostatic interactions.

The drug-loading efficiency and entrapment efficiency of the PLNPs-RSG and PLNPs-RSG-MBs complex were 30.5% and 13.9%, and 28.5% and 17.7%, respectively. When exposed to US power densities of 0, 1, and 2 W/cm^2, drug release from the PLNPs-RSG-MBs complex occurred as an initial burst within 12 h and sustained release within 48 h after the initial release. In the absence of US exposure, the release rate of RSG from the complex at 48 h was 21.2%; in contrast, when the complex

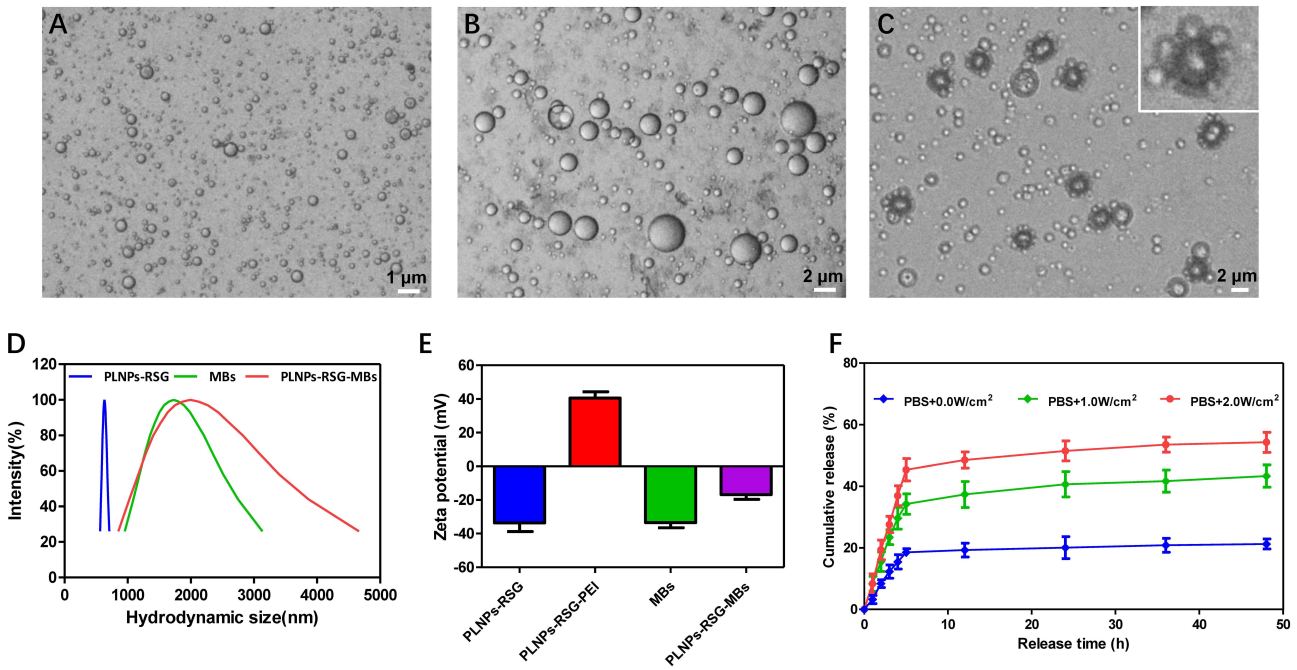

Figure 2 Characterization of the different preparations. Inverted microscope images of (**A**) PLNPs-RSG, (**B**) free MBs and (**C**) PLNPs-RSG-MBs complex. (**D**) Hydrodynamic diameter distributions of the PLNPs-RSG, free MBs and PLNPs-RSG-MBs. (**E**) Zeta potentials of the PLNPs-RSG, PLNPs-RSG-PEI, free MBs and PLNPs-RSG-MBs. (**F**) In vitro release of RSG from the PLNPs-RSG-MBs complex following exposure to US at 0, 1, and 2 W/cm^2.

was exposed to the US at power densities of 1 and 2 W/cm^2, the release rate at 48 h increased to 43.3% and 54.3%, respectively. Regarding this result, the release rate of RSG was significantly higher with US exposure than without US exposure, and the release of RSG could be controlled by adjusting the US power density (Figure 2F). This result is consistent with previous studies,[28] MBs destruction by US exposure was thought to have promoted the diffusion of nanoparticles, and the chemical structure and encapsulation stability of nanoparticles were also affected by the US force, resulting in increased drug release rates.

Cell Viability and in vivo Biocompatibility

We evaluated the cytotoxicity of PLNPs, the PLNPs-MBs complex, PLNPs-RSG and the PLNPs-RSG-MBs complex toward mouse mesangial cells (SV40-MES-13) to examine their potential for biomedical applications. After incubation with PLNPs, the PLNPs-MBs complex, PLNPs-RSG or the PLNPs-RSG-MBs complex at concentrations of up to 10 μg/mL for 24 h, the cells maintained a high viability (>90%), suggesting that PLNPs, the PLNPs-MBs complex, PLNPs-RSG and the PLNPs-RSG-MBs complex did not induce obvious cytotoxicity, indicating their excellent biocompatibility (Figure 3A).

The in vivo biocompatibility of PLNPs-RSG and the PLNPs-RSG-MBs complex was further investigated. After an intravenous injection of PLNPs-RSG or the PLNPs-RSG-MBs complex at a volume of 200 μL (15 mg/mL), the body weights of the rats in each group had not decreased significantly at day 21. In addition, no obvious acute or chronic pathological damage, inflammation, or necrosis of the major organs (heart, liver, spleen, lung, and kidney) was observed on H&E staining (Figure 3B), indicating that PLNPs-RSG and the PLNPs-RSG-MBs complex exhibited excellent biocompatibility.

Cellular Uptake

The cellular uptake of PLNPs-RSG and PLNPs-RSG-MBs was evaluated after a 6-h incubation. CLSM images showed significantly stronger intracellular fluorescence signals for PLNPs-RSG-MBs-Cy5.5 with US exposure than PLNPs-RSG-MBs-Cy5.5 without US exposure, suggesting that MBs exposed to the US increased the cellular uptake. In addition, the intracellular fluorescence of PLNPs-RSG-MBs-Cy5.5 with US exposure was higher than PLNPs-RSG-Cy5.5 with US exposure, suggesting that the cellular accumulation of nanoparticles integrated with MBs was greater than that nanoparticles without MBs upon exposure to US (Figure 4A). The quantitative

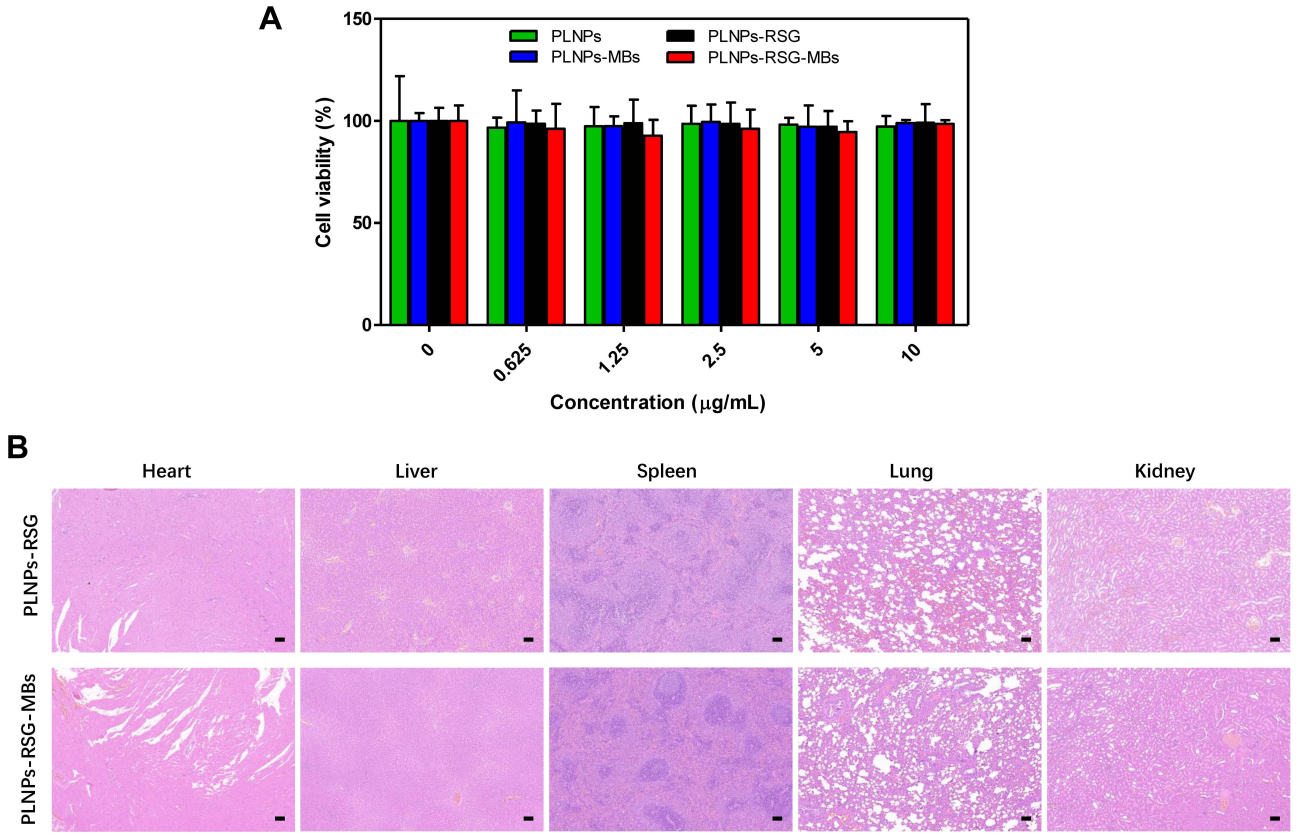

Figure 3 Cell viability and in vivo biocompatibility. (**A**) Relative viability of SV40-MES-13 cells after a 24-h incubation with the different preparations. (**B**) H&E staining of the major organs of rats injected with PLNPs-RSG or PLNPs-RSG-MBs for 21 days (100×).

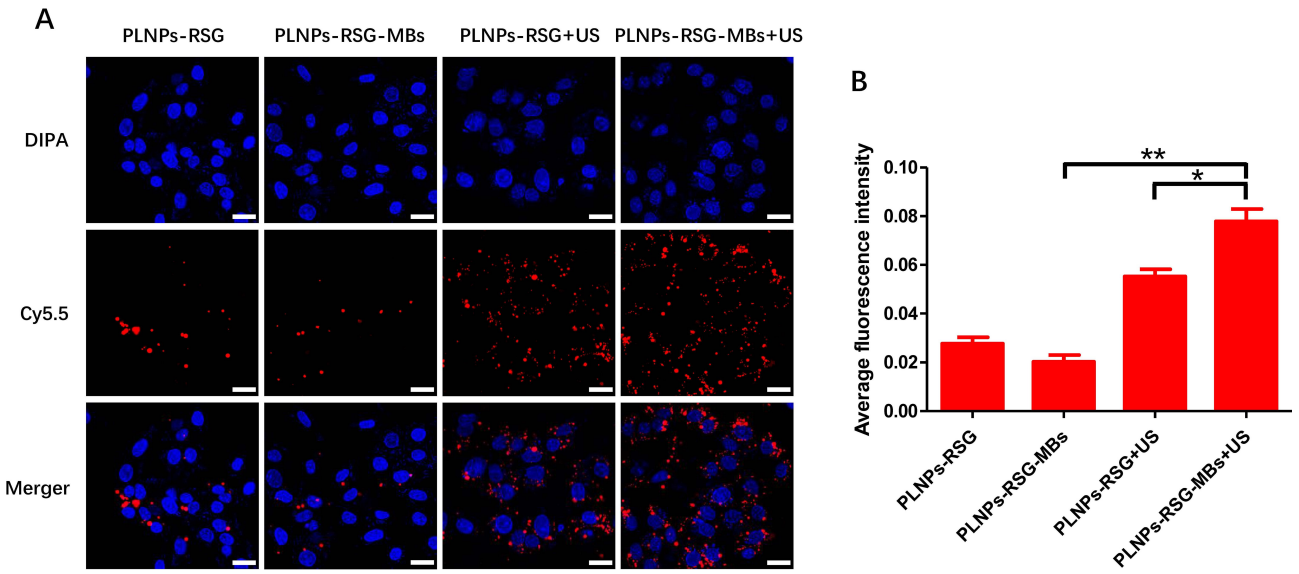

Figure 4 Cellular uptake. (**A**) CLSM images of SV40-MES-13 cells incubated with PLNPs-RSG-Cy5.5 and PLNPs-RSG-MBs-Cy5.5 with or without US exposure for 6 h (nuclei: blue, Cy5.5: red, scale bars: 25 μm). (**B**) Average fluorescence intensity of cells incubated with PLNPs-RSG-Cy5.5 and PLNPs-RSG-MBs-Cy5.5 with or without US exposure for 6 h (n=3, *p< 0.05 and **p< 0.01).

analysis of the average fluorescence intensity in these groups revealed a significantly higher level of cellular uptake of PLNPs-RSG-MBs-Cy5.5 with US exposure than PLNPs-RSG-MBs-Cy5.5 without US exposure ($p<0.01$). In addition, the cellular uptake of PLNPs-RSG-MBs-Cy5.5 with US exposure was significantly greater

than PLNPs-RSG-Cy5.5 with US exposure ($p<0.05$) (Figure 4B).

The excellent cellular uptake efficiency of nanoparticles in the PLNPs-RSG-MBs-Cy5.5 with US exposure group was potentially attributed to the mechanism known as sonoporation. US exposure increases the permeability of cell membranes; consequently, US could increase the cellular internalization of small molecules, genes, and nanoparticles.[29] Furthermore, the combination of US exposure with externally administered MBs may enhance this effect. Under the acoustic energy generated from US exposure, the destruction of MBs results in transient and nonspecific perforation of the cell membranes, leading to the accumulation of large amounts of macromolecules such as nanoparticles and drugs in cells.[30,31]

In vivo Drug Delivery and Biodistribution

On the third day after UUO, conventional US imaging showed that the obstructed kidney was markedly larger than the sham-operated kidney, and all UUO animals exhibited mild hydronephrosis. After the injection of PLNPs-RSG, there was no obvious enhancement in the kidney, while after injection of PLNPs-MBs or the PLNPs-RSG-MBs complex, the kidney parenchyma was significantly enhanced, indicating that the complex displayed a good imaging capability. Upon US exposure, the MBs were destroyed and no contrast in the kidney was observed (Figure 5A); thus, movement or rupture of the MBs in the vessels was tracked by US imaging, providing a convenient method for the real-time monitoring of delivery.

Either PLNPs-RSG-Cy5.5 or PLNPs-RSG-MBs-Cy5.5 was intravenously injected into UUO rats. To investigate the US-dependent distribution of each preparation, the rats were or were not exposed to US under the previously described conditions. Using the left kidneys as the controls, the fluorescence intensity of the right kidney (the obstructed kidney) in the PLNPs-RSG-MBs-Cy5.5 (US+) group was stronger than the PLNPs-RSG-MBs-Cy5.5 group without US exposure at 24 h after injection. In addition, PLNPs-RSG-MBs-Cy5.5 (US+) showed stronger fluorescence than PLNPs-RSG-Cy5.5 (US+) (Figure 5B and C). Quantitative analysis revealed that the relative ratio between the fluorescence intensities of the right and left kidneys in the PLNPs-RSG-MBs-Cy5.5 (US+) group was the highest among the groups ($p<0.05$) (Figure 5D). These results indicated that the targeting ability mediated by local US exposure could improve the kidney accumulation, in addition, US combined with MBs could enhance this effect, which providing a higher concentration of the drug and subsequently increasing the therapeutic efficiency and potentially minimizing side effects.[32]

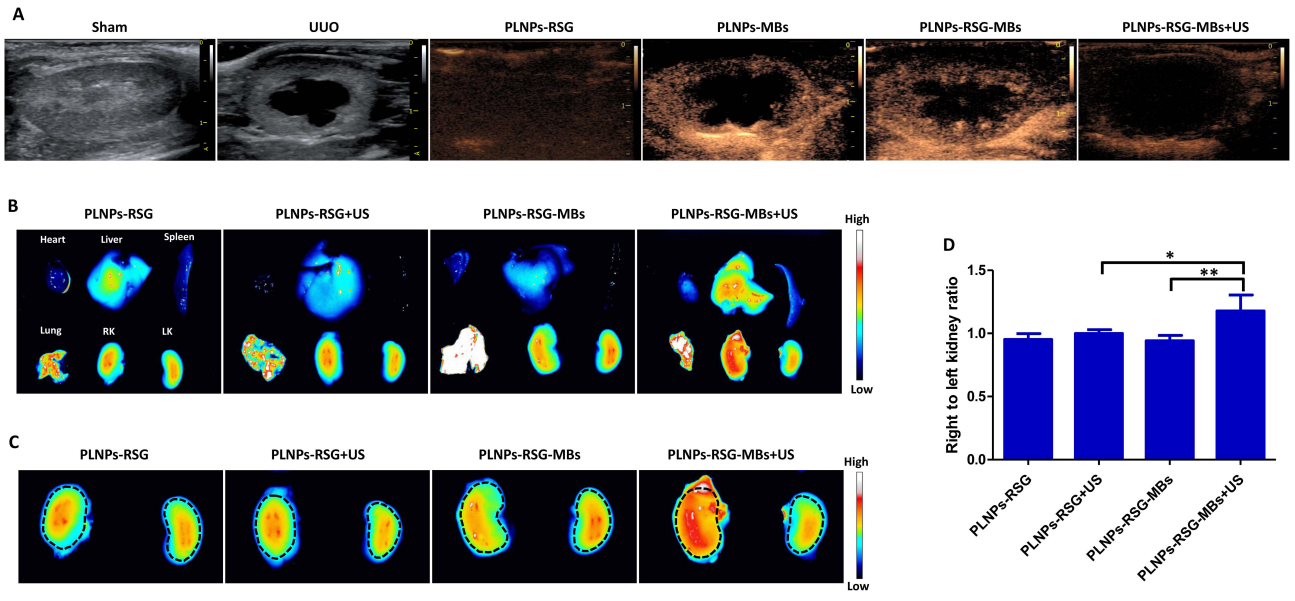

Figure 5 In vivo drug delivery and biodistribution in rats. (**A**) B-mode US images of the kidneys (sham, UUO) and CEUS images of obstructed kidneys without US exposure (PLNPs-RSG, PLNPs-MBs and PLNPs-RSG-MBs) and with US exposure (PLNPs-RSG-MBs+US). (**B**) In vivo fluorescence images of major organs from UUO rats sacrificed 24 h after the injection of PLNPs-RSG-Cy5.5 or PLNPs-RSG-MBs-Cy5.5 with or without US exposure (RK: right kidney, LK: left kidney). (**C**) In vivo fluorescence images of the right and left kidneys from all groups. (**D**) Relative fluorescence intensity in the right kidney compared to the left kidney of UUO rats in all groups (n=3, *p< 0.05 and **p< 0.01).

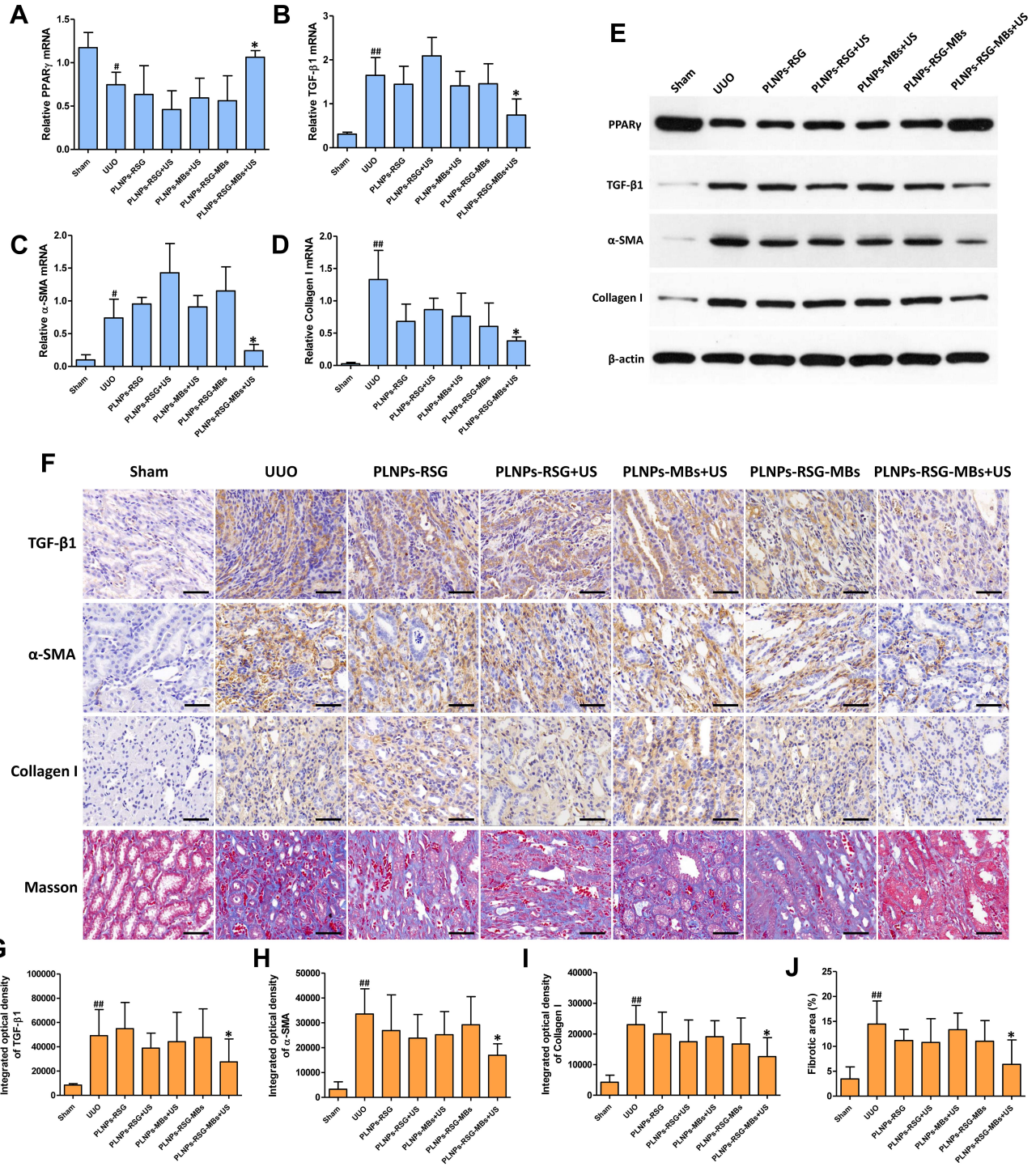

Figure 6 Antifibrotic effect in vivo. The levels of the (**A**) PPARγ, (**B**) TGF-β1, (**C**) α-SMA and (**D**) Collagen I mRNAs were detected using fluorogenic quantitative RT-PCR. (**E**) The levels of the PPARγ, TGF-β1, α-SMA and Collagen I proteins were determined using Western blot analysis. (**F**) Representative photomicrographs showing immunohistochemical staining for TGF-β1, α-SMA and Collagen I and Masson's trichrome staining in the kidneys (400×). Quantitative evaluation of immunohistochemical staining for (**G**) TGF-β1, (**H**) α-SMA and (**I**) Collagen I. (**J**) Quantitative analysis of the blue-stained area by Masson's trichrome staining (n=5, $^{\#\#}p<0.01$ and $^{\#}p<0.05$ vs the sham group, $^{*}p < 0.05$ vs the UUO group).

Antifibrotic Effect in vivo

Since RSG is an exogenous agonist of PPARγ, to investigate whether a combination of the PLNPs-RSG-MBs complex with US exposure could activate PPARγ, we first detected the levels of the PPARγ mRNA and protein in the kidneys. Antifibrotic factors, including PPAR isoforms, especially PPARγ, are downregulated following UUO.[33,34] In our study, we obtained similar results in the UUO

group. PPARγ expression was markedly downregulated in the kidneys of UUO rats but significantly upregulated in the PLNPs-RSG-MBs+US group compared with the untreated UUO group ($p< 0.05$). However, the expression of PPARγ in the other four partial treatment groups did not significantly change (Figure 6A and E). These results indicated that treatment with the PLNPs-RSG-MBs complex combined with US exposure improved the efficiency of drug delivery into the kidney tissue and contributed to activating PPARγ, consistent with the in vivo biodistribution results.

We further investigated the expression of some profibrotic markers, such as TGF-β1, α-SMA and Collagen I, in the kidney. Fluorogenic quantitative RT-PCR and Western blot analysis were performed to measure the levels of the TGF-β1, α-SMA and Collagen I mRNAs and proteins in the kidney, respectively. The levels of TGF-β1, α-SMA and Collagen I were significantly upregulated after the UUO operation ($p< 0.05$). In many models of renal injuries, including UUO, an increase in TGF-β1 production is one of the prominent markers of ongoing renal fibrosis.[35] In addition, UUO induces the expression of α-SMA in the renal tubular interstitium, which is a well-known hallmark of myofibroblast formation,[36] and increases collagen deposition. After treatment, the expression of TGF-β1, α-SMA and Collagen I was significantly decreased in the PLNPs-RSG-MBs+US group ($p< 0.05$); however, no significant difference in the expression of these markers was observed in the other four partial treatment groups (Figure 6B–E). In addition, immunohistochemical staining displayed a pattern similar to the results of the fluorogenic quantitative RT-PCR and Western blot analysis; UUO significantly increased the expression of TGF-β1, α-SMA and Collagen I in obstructed kidneys when compared with their expression in the sham group ($p< 0.01$). After treatment, the expression of TGF-β1, α-SMA and Collagen I in the PLNPs-RSG-MBs+US group was significantly decreased ($p< 0.05$); however, the expression of these markers in the other four partial treatment groups was unchanged (Figure 6F–I).

Masson's trichrome staining was performed to further investigate the antifibrotic effect on the kidney histology. After the UUO operation, abundant mature collagen fibers were stained blue in the obstructed kidneys, indicating interstitial fibrosis. After treatment with the PLNPs-RSG-MBs complex and US exposure, a significant reduction in the blue staining intensity was observed in the PLNPs-RSG-MBs+US group ($p< 0.05$), suggesting the attenuation of collagen deposition; however, no significant difference in the blue staining intensity was observed in the other four partial treatment groups compared with the untreated UUO group (Figure 6F and J).

Conclusion

In this study, we developed a novel RSG-loaded PLNPs-MBs complex. This complex possessed a good uniformity and dispersity, high drug-loading capacity, US-responsive drug release, excellent biocompatibility both in vitro and in vivo, and higher cellular uptake efficiency in vitro and kidney-targeting ability in vivo. Moreover, the combination of the PLNPs-RSG-MBs complex with US exposure significantly reduced collagen deposition and successfully attenuated renal fibrosis in a UUO rat model. The use of this complex with US exposure may be a promising approach for the treatment of RIF.

Ethics and Consent Statement

This study received ethical approval from the Laboratory Animal Ethics Committee of Jinling Hospital, Medical School of Nanjing University (approval No. 2017JLHGKJDWLS-0817).

Acknowledgments

This work was supported by a grant from the National Natural Science Foundation of China (No. 81701722)

Disclosure

The authors declare that they have no conflicts of interest for this work.

References

1. Kiss-Toth E, Roszer T. PPARgamma in kidney physiology and pathophysiology. *PPAR Res*. 2008;2008183108. doi:10.1155/2008/183108
2. Zhang ZH, He JQ, Zhao YY, et al. Asiatic acid prevents renal fibrosis in UUO rats via promoting the production of 15d-PGJ2, an endogenous ligand of PPAR-gamma. *Acta Pharmacol Sin*. 2020;41(3):373–382. doi:10.1038/s41401-019-0319-4
3. Kusunoki H, Taniyama Y, Rakugi H, et al. Cardiac and renal protective effects of irbesartan via peroxisome proliferator-activated receptor gamma-hepatocyte growth factor pathway independent of angiotensin II Type 1a receptor blockade in mouse model of salt-sensitive hypertension. *J Am Heart Assoc*. 2013;2(2):e000103. doi:10.1161/JAHA.113.000103
4. Kawai T, Masaki T, Doi S, et al. PPAR-gamma agonist attenuates renal interstitial fibrosis and inflammation through reduction of TGF-beta. *Lab Invest*. 2009;89(1):47–58. doi:10.1038/labinvest.2008.104
5. Wang Z, Liu Q, Dai W, et al. Pioglitazone downregulates Twist-1 expression in the kidney and protects renal function of Zucker diabetic fatty rats. *Biomed Pharmacother*. 2019;118109346. doi:10.1016/j.biopha.2019.109346.

6. Friedland SN, Leong A, Filion KB, et al. The cardiovascular effects of peroxisome proliferator-activated receptor agonists. *Am J Med*. 2012;125(2):126–133. doi:10.1016/j.amjmed.2011.08.025
7. Colmers IN, Bowker SL, Majumdar SR, et al. Use of thiazolidinediones and the risk of bladder cancer among people with type 2 diabetes: a meta-analysis. *CMAJ*. 2012;184(12):E675–683. doi:10.1503/cmaj.112102
8. Kopechek JA, McTiernan CF, Chen X, et al. Ultrasound and microbubble-targeted delivery of a microRNA inhibitor to the heart suppresses cardiac hypertrophy and preserves cardiac function. *Theranostics*. 2019;9(23):7088–7098. doi:10.7150/thno.34895
9. Horsley H, Owen J, Browning R, et al. Ultrasound-activated microbubbles as a novel intracellular drug delivery system for urinary tract infection. *J Control Release*. 2019;301166–301175. doi:10.1016/j.jconrel.2019.03.017.
10. Huang S, Ren Y, Wang X, et al. Application of ultrasound-targeted microbubble destruction-mediated exogenous gene transfer in treating various renal diseases. *Hum Gene Ther*. 2019;30(2):127–138. doi:10.1089/hum.2018.070
11. Fan Z, Kumon RE, Deng CX. Mechanisms of microbubble-facilitated sonoporation for drug and gene delivery. *Ther Deliv*. 2014;5(4):467–486. doi:10.4155/tde.14.10
12. Li P, Gao Y, Zhang J, et al. Renal interstitial permeability changes induced by microbubble-enhanced diagnostic ultrasound. *J Drug Target*. 2013;21(5):507–514. doi:10.3109/1061186X.2013.776053
13. Zhang Y, Ye C, Xu Y, et al. Ultrasound-mediated microbubble destruction increases renal interstitial capillary permeability in early diabetic nephropathy rats. *Ultrasound Med Biol*. 2014;40(6):1273–1281. doi:10.1016/j.ultrasmedbio.2013.12.006
14. Li P, Zheng Y, Ran H, et al. Ultrasound triggered drug release from 10-hydroxycamptothecin-loaded phospholipid microbubbles for targeted tumor therapy in mice. *J Control Release*. 2012;162(2):349–354. doi:10.1016/j.jconrel.2012.07.009
15. Jamburidze A, Huerre A, Baresch D, et al. Nanoparticle-coated microbubbles for combined ultrasound imaging and drug delivery. *Langmuir*. 2019;35(31):10087–10096. doi:10.1021/acs.langmuir.8b04008
16. Tay LM, Xu C. Coating microbubbles with nanoparticles for medical imaging and drug delivery. *Nanomedicine (Lond)*. 2017;12(2):91–94. doi:10.2217/nnm-2016-0362
17. Lee JH, Moon H, Han H, et al. Antitumor effects of intra-arterial delivery of albumin-doxorubicin nanoparticle conjugated microbubbles combined with ultrasound-targeted microbubble activation on VX2 rabbit liver tumors. *Cancers (Basel)*. 2019;11(4):581. doi:10.3390/cancers11040581
18. Lv Y, Cao Y, Li P, et al. Ultrasound-triggered destruction of folate-functionalized mesoporous silica nanoparticle-loaded microbubble for targeted tumor therapy. *Adv Healthc Mater*. 2017;6(18):1700354. doi:10.1002/adhm.201700354
19. Geng X, Zhang M, Lai X, et al. Small-sized cationic miRi-PCNPs selectively target the kidneys for high-efficiency antifibrosis treatment. *Adv Healthc Mater*. 2018;7(21):e1800558. doi:10.1002/adhm.201800558
20. Gu P, Wusiman A, Wang S, et al. Polyethylenimine-coated PLGA nanoparticles-encapsulated Angelica sinensis polysaccharide as an adjuvant to enhance immune responses. *Carbohydr Polym*. 2019;223115128. doi:10.1016/j.carbpol.2019.115128.
21. Salvador A, Sandgren KJ, Liang F, et al. Design and evaluation of surface and adjuvant modified PLGA microspheres for uptake by dendritic cells to improve vaccine responses. *Int J Pharm*. 2015;496(2):371–381. doi:10.1016/j.ijpharm.2015.10.037
22. Yu K, Zhao J, Zhang Z, et al. Enhanced delivery of Paclitaxel using electrostatically-conjugated Herceptin-bearing PEI/PLGA nanoparticles against HER-positive breast cancer cells. *Int J Pharm*. 2016;497(1–2):78–87. doi:10.1016/j.ijpharm.2015.11.033
23. Ja'afar F, Leow CH, Garbin V, et al. Surface charge measurement of SonoVue, definity and optison: a comparison of laser doppler electrophoresis and micro-electrophoresis. *Ultrasound Med Biol*. 2015;41(11):2990–3000. doi:10.1016/j.ultrasmedbio.2015.07.001
24. Fan CH, Wang TW, Hsieh YK, et al. Enhancing boron uptake in brain glioma by a boron-polymer/microbubble complex with focused ultrasound. *ACS Appl Mater Interfaces*. 2019;11(12):11144–11156. doi:10.1021/acsami.8b22468
25. Coombes AG, Yeh MK, Lavelle EC, et al. The control of protein release from poly(DL-lactide co-glycolide) microparticles by variation of the external aqueous phase surfactant in the water-in oil-in water method. *J Control Release*. 1998;52(3):311–320. doi:10.1016/s0168-3659(98)00006-6
26. Qiao H, Sun M, Su Z, et al. Kidney-specific drug delivery system for renal fibrosis based on coordination-driven assembly of catechol-derived chitosan. *Biomaterials*. 2014;35(25):7157–7171. doi:10.1016/j.biomaterials.2014.04.106
27. Wei S, Xu C, Rychak JJ, et al. Short hairpin RNA knockdown of connective tissue growth factor by ultrasound-targeted microbubble destruction improves renal fibrosis. *Ultrasound Med Biol*. 2016;42(12):2926–2937. doi:10.1016/j.ultrasmedbio.2016.07.022
28. Wang J, Li P, Tian R, et al. A novel microbubble capable of ultrasound-triggered release of drug-loaded nanoparticles. *J Biomed Nanotechnol*. 2016;12(3):516–524. doi:10.1166/jbn.2016.2181
29. Zhou QL, Chen ZY, Wang YX, et al. Ultrasound-mediated local drug and gene delivery using nanocarriers. *Biomed Res Int*. 2014;2014963891. doi:10.1155/2014/963891.
30. Karshafian R, Bevan PD, Williams R, et al. Sonoporation by ultrasound-activated microbubble contrast agents: effect of acoustic exposure parameters on cell membrane permeability and cell viability. *Ultrasound Med Biol*. 2009;35(5):847–860. doi:10.1016/j.ultrasmedbio.2008.10.013
31. Han H, Lee H, Kim K, et al. Effect of high intensity focused ultrasound (HIFU) in conjunction with a nanomedicines-microbubble complex for enhanced drug delivery. *J Control Release*. 2017;26675–26686. doi:10.1016/j.jconrel.2017.09.022.
32. Bressand D, Novell A, Girault A, et al. Enhancing nab-paclitaxel delivery using microbubble-assisted ultrasound in a pancreatic cancer model. *Mol Pharm*. 2019;16(9):3814–3822. doi:10.1021/acs.molpharmaceut.9b00416
33. Kim J, Imig JD, Yang J, et al. Inhibition of soluble epoxide hydrolase prevents renal interstitial fibrosis and inflammation. *Am J Physiol Renal Physiol*. 2014;307(8):F971–980. doi:10.1152/ajprenal.00256.2014
34. Kim J, Yoon SP, Toews ML, et al. Pharmacological inhibition of soluble epoxide hydrolase prevents renal interstitial fibrogenesis in obstructive nephropathy. *Am J Physiol Renal Physiol*. 2015;308(2):F131–139. doi:10.1152/ajprenal.00531.2014
35. El Chaar M, Chen J, Seshan SV, et al. Effect of combination therapy with enalapril and the TGF-beta antagonist 1D11 in unilateral ureteral obstruction. *Am J Physiol Renal Physiol*. 2007;292(4):F1291–1301. doi:10.1152/ajprenal.00327.2005
36. Rao KB, Malathi N, Narashiman S, et al. Evaluation of myofibroblasts by expression of alpha smooth muscle actin: a marker in fibrosis, dysplasia and carcinoma. *J Clin Diagn Res*. 2014;8(4):ZC14–17. doi:10.7860/JCDR/2014/7820.4231